Potential of Sample Migration and Explainable Machine Learning Model for Monitoring Spatiotemporal Changes of Wetland Plant Communities

Kaidong Feng, Dehua Mao, Jianing Zhen, Haiguang Pu, Hengqi Yan, Ming Wang, Duanrui Wang, Hengxing Xiang, Yongxing Ren, Ling Luo, and Zongming Wang

***Abstract*—The composition and dynamics of wetland plant communities play a critical role in maintaining the functionality of wetland ecosystems and serve as important indicators of wetland degradation and restoration. Accurately identifying wetland plant communities using remote sensing techniques remains challenging due to the complex environment and cloud contamination. Here, we applied a sample migration method based on change vector analysis and a random forest (RF) classifier incorporating SHapley Additive exPlanations (SHAP) to explore the spatiotemporal changes of wetland plant communities in the western Songnen Plain of China between 2016 and 2022, and to better understand the decision logic of the RF model. Our work achieved accurate annual wetland classification at the community scale, with an average overall accuracy of 89.5% and an average kappa coefficient of 0.87. Our analysis revealed different spatiotemporal change characteristics of wetland plant communities in the western Songnen Plain and three national nature reserves. The SHAP model showed that MOS_IRECI is the most important feature determining the prediction results of the RF model, and the importance of the features differs at global and local levels. This study confirms the feasibility of annual dynamic monitoring of wetland plant communities at a regional scale. The results are expected to provide a reference for the fine and sustainable management of wetland resources in the western Songnen Plain, as well as valuable data support for related wetland ecology research.**

***Index Terms*—Google Earth engine (GEE), random forest (RF), sample migration, SHapley Additive exPlanations (SHAP), wetland plant communities.**

Manuscript received 13 February 2024; revised 1 April 2024; accepted 7 May 2024. Date of publication 13 May 2024; date of current version 30 May 2024. This work was supported in part by the National Natural Science Foundation of China under Grant 42301429, Grant 42101379, and Grant 42101399, and in part by the Natural Science Foundation of Jilin Province under Grant YDZJ202301ZYTS218. *(Corresponding author: Jianing Zhen.)*

Kaidong Feng, Haiguang Pu, Ming Wang, and Duanrui Wang are with the State Key Laboratory of Black Soils Conservation and Utilization, Northeast Institute of Geography and Agroecology, Chinese Academy of Sciences, Changchun 130102, China, and also with the University of Chinese Academy of Sciences, Beijing 100049, China (e-mail: fengkaidong20@mails.ucas.ac.cn; puhaiguang20@mails.ucas.ac.cn; w.m9047@163.com; wangduanrui21@mails.ucas.ac.cn).

Dehua Mao, Jianing Zhen, Hengxing Xiang, Yongxing Ren, and Ling Luo are with the State Key Laboratory of Black Soils Conservation and Utilization, Northeast Institute of Geography and Agroecology, Chinese Academy of Sciences, Changchun 130102, China (e-mail: maodehua@iga.ac.cn; zhenjianing@iga.ac.cn; xianghengxing@iga.ac.cn; renyongxing@iga.ac.cn; luoling@iga.ac.cn).

Hengqi Yan is with the Jilin Earthquake Agency, Changchun 130117, China (e-mail: 1570061018@qq.com).

Zongming Wang is with the State Key Laboratory of Black Soils Conservation and Utilization, Northeast Institute of Geography and Agroecology, Chinese Academy of Sciences, Changchun 130102, China, and also with the National Earth System Science Data Center, Beijing 100101, China (e-mail: zongmingwang@iga.ac.cn).

Digital Object Identifier 10.1109/JSTARS.2024.3399791

I. Introduction

WETLAND plant communities exhibit changes over time as they adapt to a dynamic environment, which is shaped by factors such as plant traits (e.g., reproductive strategies and competition), disturbances (e.g., grazing, fire, and nutrient inputs from adjacent land uses), climate (e.g., temperature and precipitation), and hydrological changes (e.g., salinity and inundation) to ensure the proper functioning of the wetland ecosystem [1], [2]. The composition and dynamics of wetland plant communities are crucial indicators of wetland degradation and restoration [3], [4]. Therefore, identifying and analyzing wetland plant communities over time is essential for diagnosing the health of wetland ecosystems and provides valuable guidance for scientific conservation and restoration of existing wetlands.

Although remote sensing has been widely used in wetland change detection [5], [6], [7], classifying wetland plant communities using remote sensing remains challenging due to the dynamic and complex nature of wetland environments [8], [9]. Selecting suitable remote sensing data, implementing robust methods, and obtaining reliable sample data are the key technical challenges that affect the classification accuracy of wetland plant communities [10]. Researchers have conducted extensive studies using different remote sensing data to identify wetland plant communities worldwide [11], [12], [13], [14]. This is attributed to the diverse features of different sensors, which allow community types to be distinguished from different perspectives. For large-scale classification of plant communities, integrating optical and radar data, such as the Sentinel-1/2, offers numerous advantages [15], [16]. These include cost-effectiveness compared to studies based on hyperspectral data [17], richer feature information than studies based on a single data source [18], and effective mitigation of the impact of clouds and cloud shadows [19]. In addition, some studies also incorporate digital elevation models (DEMs) into the classification

process to improve accuracy [20]. Unlike single-date imagery, time-series data can capture seasonal variations in wetland plant communities and mitigate the impact of anomalous disturbances [18]. For example, phenological parameters can be extracted from the time-series curves of Sentinel-2 imagery, which are considered powerful features for community classification and have been widely used in recent studies [21]. The annual mean composite images from Sentinel-1 time-series data show the general change situation within one year and avoid the influence of hydrological fluctuations on wetland vegetation [22]. The combination of Sentinel-1/2 time-series data and DEM can compensate for the limitations of individual data sources and provide multidimensional classification features that improve the accuracy of wetland plant community classification. Combining multisource remote sensing data to explore the feasibility of fine wetland plant community distribution and dynamics on a broader scale is of great significance [8], [23].

Several artificial intelligence algorithms, including traditional machine learning (ML) algorithms such as iterative self-organizing data analysis techniques algorithm (ISODATA), decision trees (DTs), and random forests (RFs), as well as deep learning (DL) algorithms developed in recent years, have been applied to wetland plant community classification [24], [25]. DL has the advantages of automatic feature learning and powerful data fitting capabilities, which can help to improve classification accuracy [26], [27]. However, challenges in wetland plant community research such as difficulties in sample collection and limited sample numbers have posed obstacles to constructing accurate DL models [11]. In addition, the highly nonlinear operations involved in DL models make the results difficult to interpret, limiting their suitability for wetland plant community classification [28]. The RF algorithm is widely used because of its powerful and flexible ability to handle complex data with varying dimensions and nonlinearity [29], [30]. In recent years, numerous studies in terms of wetland mapping across different scales and species have been carried out based on the RF classifier [16], [20], [31], [32], [33], [34], which has fully proved its effectiveness and robustness. However, all these studies lack deep analysis of the decision logic and feature importance of the RF classifier, which is detrimental to reviewing whether the model output results are reasonable. As a relatively versatile model interpretability method, the SHapley Additive exPlanations (SHAP) can interpret black-box models at both global and local levels [35]. Therefore, combining the RF classifier with SHAP can help improve the accuracy and interpretability of wetland plant community classification.

Obtaining accurate and sufficient sample data is a critical prerequisite for accurate mapping of wetland plant communities [33]. For road-inaccessible wetlands, field surveys can only obtain a limited amount of sample data, typically gathered at the wetlands' edge. Visual interpretation based on high-resolution imagery is only effective when field sample data is available as a reference. To overcome this challenge, some studies have utilized sample migration methods based on change detection to rapidly obtain an accurate sample dataset for non-surveyed years and regions [36]. Among these methods, change vector analysis (CVA), which is derived from the image difference technique,

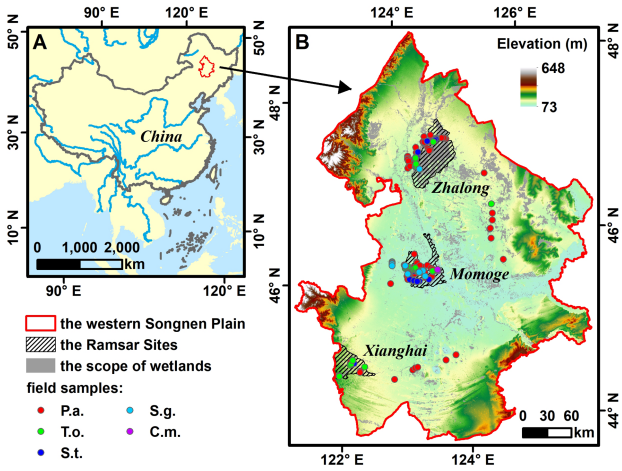

Fig. 1. General location of the study area. (a) Geographical location of the western Songnen Plain in China. (b) Distribution of the Ramsar Sites, scope of wetlands, and field samples shown on a DEM map of the western Songnen Plain.

is the most widely used [37], [38], [39]. To reduce information redundancy, some studies use spectral transformation techniques to reduce data dimensions before performing change detection [40]. As the three primary components obtained from the K-T transformation have distinct physical meanings and correspond to soil, vegetation, and moisture information, it is considered more favorable than principal component analysis for wetland plant monitoring [41], [42]. However, the effectiveness of using the CVA method based on the principal components of the K-T transformation for wetland plant community sample migration is still unverified.

In recent years, numerous wetland conservation and restoration measures have been implemented in the western Songnen Plain [43]. However, the effectiveness of these wetland management strategies remains inadequate due to limited foundational data on the composition and changes in wetland plant communities. To address these issues, this study aims to:

1) obtain migration sample data from 2016 to 2021 using 2022 samples;
2) achieve the annual classification of wetland plant communities in the western Songnen Plain from 2016 to 2022 on the Google Earth engine (GEE);
3) interpret the decision logic of the RF model; and
4) analyze the spatiotemporal changes of different wetland plant communities in the western Songnen Plain and three national nature reserves.

II. Materials and Methods

A. Study Area

The western Songnen Plain is located in northeast China [see Fig. 1(a)] and is formed by the alluvial deposits of the Songhua river, Nen river, and their tributaries, covering an area of 10.2×10^4 km^2 [44]. The wetland ecosystems in this region with complex structures and unique functions are essential for

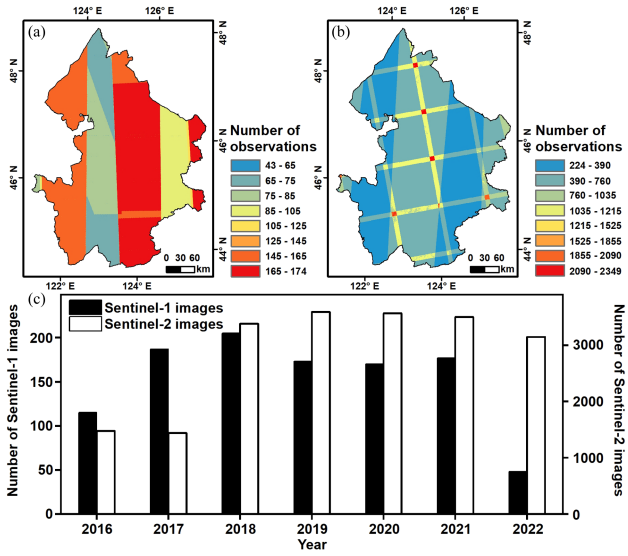

Fig. 2. Spatial distribution and histogram of all available Sentinel-1/2 images number. Spatial distribution of all available observations over the (a) western Songnen Plain by Sentinel-1 and (b) Sentinel-2 from 2016 to 2022. (c) Histogram shows the number of Sentinel-1/2 images acquired each year.

the ecological security of northeast China and the East Asian-Australasian Flyway [45]. The main types of plant communities are *Phragmites australis* (*P.a.*), *Typha orientalis* (*T.o.*), *Scirpus triquater* (*S.t.*), *Suaeda glauca* (*S.g.*), and *Carex meyeriana* (*C.m.*), which provide habitats and food sources for many rare migratory birds, such as Oriental White Stork, Grus japonensis, and Grus leucogeranus, etc. [46], [47], [48]. Currently, the National Forestry and Grassland Administration of China has established five national nature reserves here, among which Zhalong, Xianghai, and Momoge have been included in the Ramsar Site List of Wetlands [49] [see Fig. 1(b)].

B. Datasets

1) Remote Sensing Imagery: The remote sensing imagery used in this study comprises Sentinel-1, Sentinel-2, and DEM. Specifically, all available Sentinel-2 images covering the study area from 2016 to 2022 were used. The L2A level Sentinel-2 images are from 2019 to 2022, whereas the L1C level Sentinel-2 images are from 2016 to 2018. In 2016 and 2017, about 1400 images were acquired each year. However, with the release of Sentinel-2B data, the number of images acquired each year has increased to about 3500 since 2018 (see Fig. 2). The preprocessing of Sentinel-2 images mainly encompassed image clipping, cloud pixel masking, and calculation of normalized difference vegetation index (NDVI), inverted red-edge chlorophyll index (IRECI), and normalized difference water index (NDWI) of all images to construct the original time-series stack. Sentinel-1 images were used from May to October because this is the growing season for most vegetation in the study area. The number of Sentinel-1 images acquired each year is shown in Fig. 2. It should be noted that Sentinel-1B malfunctioned on December 23, 2021, causing incomplete coverage of the study area in the Sentinel-1 images acquired in 2022. In this study, the only preprocessing required for Sentinel-1 images was speckle noise removal using a "refined Lee" filter with a 7×7 window [50]. The DEM used in this study is called "ALOS_DEM_12," obtained from PIE-Engine. It was resampled to a 10-m spatial resolution and reprojected to the "WGS 1984" coordinate system.

2) Field Sample Data: The field survey was conducted in mid-July 2022, with survey sites mainly located in Xianghai, Momoge, and Zhalong national nature reserves. Using GVG software [51], a total of 1255 sample points of various types were obtained, including 655 wetland sample points. The sample numbers for *P.a.*, *T.o.*, *S.t.*, *S.g.*, and *C.m.* communities were 323, 125, 43, 38, and 24, respectively. In addition, 93 and 9 sample points were collected from paddy fields and other wetland types, respectively. As shown in Fig. 1(b), the original samples were extremely unevenly distributed, which would affect the classification accuracy. To address this, we combined the NDVI time-series curve characteristics to expand and balance the samples by comparing the spectral differences of wetland plant communities on multispectral remote sensing images across different seasons.

C. Methods

Sample migration from 2016 to 2021 was achieved using samples collected during the field survey in 2022 and a sample migration method based on change detection. An RF model based on multisource and multitemporal remote sensing data was then used for annual wetland plant community classification. Based on the annual classification results, we analyzed the spatiotemporal change characteristics of different wetland plant communities. The general framework is shown in Fig. 3.

1) Sample Migration: The year 2022 served as the reference time node, and the sample data from 2016 to 2021 were obtained through the sample migration method based on CVA after K-T transformation, using the Sentinel-2 images and 2022 samples. To achieve change detection, it is necessary to ensure consistent radiation conditions between the reference and target year images. However, this condition is difficult to fully achieve due to the influence of clouds and shadow pixels. Thus, cloud masking, clipping, and band extraction were performed on all images with less than 20% cloud cover from June 15 to August 15. Next, the median reduction method was used to obtain cloud-free annual images with relatively consistent radiation and vegetation growth conditions. Based on the median image obtained through the above process, the K-T transformation method was performed to derive the brightness, greenness, and wetness feature images for the reference and target years, respectively.

The feature image of the reference year was defined as $A = \{X_i^j\}_{i=n}^{j=m}$ and the target year was defined as $B = \{Y_i^j\}_{i=n}^{j=m}$, where m is the pixel number and n is the band number ($n = 1, 2, 3$). To identify pixels that have not changed between the two images, the CVA method was used to obtain the change intensity (CI) information from the A image to the B image. The difference among each band of the A and B images was calculated by the following formula:

$$\Delta_i^j = A - B = X_i^j - Y_i^j. \tag{1}$$

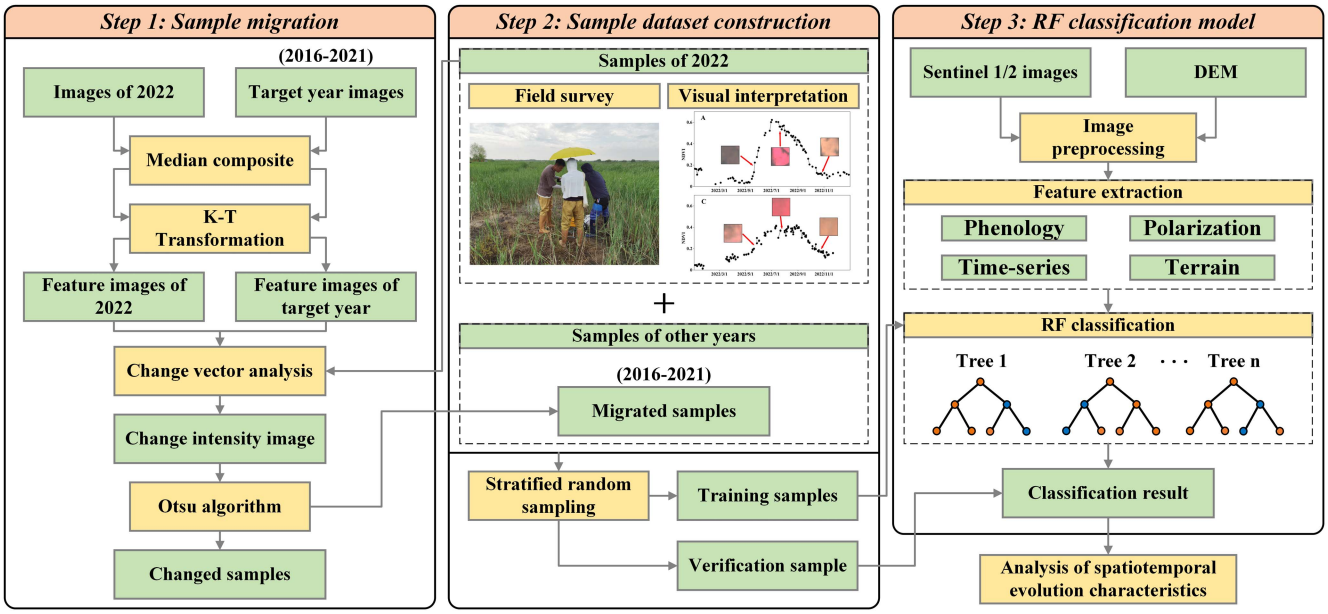

Fig. 3. General framework of this study.

The Euclidean distance of the difference band was defined as the variation intensity value as follows:

$$\rho^j = \sqrt{\sum_{i=1}^{3} (\Delta_i^j)^2}. \tag{2}$$

A threshold for ρ^j was established to binarize the change-intensity image, thereby dividing the image into changed and unchanged areas. The Otsu algorithm, an adaptive threshold segmentation method that obtains the optimal segmentation threshold by maximizing the inter-class variance, was used to determine this threshold [52]. However, results obtained using the Otsu algorithm across the entire study area may not accurately reflect the variation of sample pixels. Therefore, the Otsu algorithm was only applied to pixels corresponding to the 2022 sample data, and samples corresponding to unchanged type pixels were migrated to the target year.

2) Classification of Wetland Plant Communities: Water, artificial surfaces, and bare land do not have distinct phenological characteristics and are easily distinguished from vegetation. To simplify the classification system and reduce computational effort, a rule-based approach was utilized to exclude the nonvegetation types. We selected 300 sample points each of water, vegetation, and other types (artificial surface and bare land) based on the greenest enhanced vegetation index (EVI) and NDVI images in 2022. Extraction rules for the vegetation distribution area were defined as EVI>0.2 and NDVI>0.2 according to the frequency distribution histogram. Subsequently, a mature RF model incorporating phenological, time-series, polarization, and terrain features was employed for classification. Phenological and time-series features were derived from the Sentinel-2 NDVI, IRECI, and NDWI time-series curves, which were fitted with a two-term Fourier function (3). The polarization features were extracted from the annual median Sentinel-1 imagery, while the terrain features were extracted from DEM data. The details of the feature vectors used in the model training and classification are shown in Table I

$$y_t = \beta_0 + \beta_1 \cos(wt) + \beta_2 \sin(wt) + \beta_3 \cos(2wt) + \beta_4 \sin(2wt) + e_t. \tag{3}$$

The maximum number of features and the number of DTs are the two crucial initial parameters that require manual determination for the RF classification model. We set the maximum number of selected features for node splitting as the square root of the total number of features. This enabled the classifier to focus on training unique classification rules in each DT, reducing overall computation and preventing similar results. Following testing of the training effect of the classification model with different numbers of DTs using the 2022 sample data, we selected 25 DTs to maximize the training accuracy of the model.

The stratified random sampling method was used to divide all the samples into two parts, of which 60% were training samples and 40% were validation samples. The accuracy of the classification results was evaluated using the confusion matrix and kappa coefficient. From the confusion matrix, overall accuracy (OA), user's accuracy (UA), and producer's accuracy (PA) can be determined [53]. OA represents the ratio of correctly classified samples to the total number of samples, providing an overall measure of accuracy across all classes. The UA refers to the proportion of correct classifications among the classification results, whereas the PA refers to the proportion of correct classifications in the real situation.

3) Model Interpretation: SHAP is a game-theoretic method that explains the black-box model at both the global and local levels by computing the marginal contribution of each feature to the model output [35]. In the SHAP model, the model generates a prediction value for each sample, and the "SHAP value"

TABLE I
COLLECTION OF CLASSIFICATION FEATURE VECTORS

Source	Feature type	Feature name	Description
Sentinel-2	Phenology	SOS	Time for the start of the season
		EOS	Time for the end of the season
		MOS	Time for the middle season
		LOS	Length of the season
		BV	Base level
		SA	Seasonal amplitude
		IRS	Increase rate of the season
		DRS	Decrease rate of the season
	Time-series	BV	Base level
		BVD	Time of the base level
		MV	Maximum value
		MOS	Time for the middle season
		SA	Seasonal amplitude
Sentinel-1	Polarization	VV	Vertical-vertical backscatter
		VH	Vertical-horizontal backscatter
		SAR_{sum}	VH+VV
		SAR_{diff}	VH-VV
		SAR_{NDVI}	(VH-VV) / (VH+VV)
DEM	Terrain	ELE	Elevation
		Slope	

Note: Phenology and time-series features need to be distinguished with a suffix ("_NDVI", "_IRECI", or "_NDWI").

of the model output is the important value assigned to each feature in that sample [54]. In this study, the SHAP package (version 0.43.0) was first imported into Python 3.11.5. The "TreeExplainer" method [55] was used to interpret the output of the trained 2022 RF model. Finally, we illustrated the global importance of features, the impact of features on predicting *P.a.*, the overall substructure of a sample collection, and the contribution of each feature in a single sample to the outcome prediction using the SHAP values of the validation samples through bar, beeswarm, heatmap, and waterfall plots.

4) Spatiotemporal Change Analysis: The spatiotemporal change characteristics of different wetland plant communities in the western Songnen Plain from 2016 to 2022 were analyzed based on annual spatial distribution data using the indicators of area change, dynamic degree (DD), and CI. The DD can provide insight into the average rate of change and trend of land surface cover types over a certain period [56]. The formula for the single dynamic index is as follows:

$$\mathrm{DD} = (Y_{i2} - Y_{i1}) \,/\, Y_{i1} \times 1 \,/\, T \tag{4}$$

where *i1* is the start time; *i2* is the end time; Y_{i1} is the area at the start time; Y_{i2} is the area at the end time; and T is the length of the time interval. Each pixel identified as a wetland plant community in each year was set to 1, otherwise 0. Then,

TABLE II
SAMPLE NUMBER OF WETLAND PLANT COMMUNITIES FROM 2016 TO 2022

	P.a.	*T.o.*	*S.t.*	*S.g.*	*C.m.*
2022	221	224	232	188	203
2021	135	188	214	173	193
2020	132	201	214	163	139
2019	149	203	217	187	110
2018	157	182	219	160	120
2017	157	160	214	121	119
2016	134	153	186	120	124

the per-pixel CI of this community is calculated by the following formula:

$$\mathrm{CI} = \sum_{i=2016}^{2022} V_i \tag{5}$$

where i is the year, from 2016 to 2022; V_i is the pixel value for year i, 0 or 1. A lower value of CI indicates the presence of more intense community change, whereas a higher value suggests a more stable community structure.

III. RESULTS

A. Performance of Sample Migration Method

The CI maps of different years displayed varying distributions in the histograms of the sample pixels (see Fig. 4). The histogram was an approximately normal distribution with a peak value of about 0.3 from 2019 to 2021 (see Fig. 4), whereas it was a positively skewed distribution with a peak of about 0.05 from 2016 to 2018 (see Fig. 4). Therefore, the segmentation thresholds determined by the Otsu algorithm also varied. The threshold value from 2019 to 2021 was roughly 0.4, whereas the threshold value from 2016 to 2018 was around 0.2. The sample migration was conducted on an annual basis, utilizing the segmentation threshold of the sample pixels. Sample pixels with a CI below the threshold were considered unchanged, while those with a value above the threshold were removed. The results showed that most sample data can be retained, thereby satisfying the classification requirements. This phenomenon is in line with empirical evidence, as most land cover types tend to exhibit relative stability in the short term. Specifically, 65.9% of samples were retained in 2016, which was the year with the lowest number of unchanged samples among the six years (see Fig. 4). Conversely, the proportion of unchanged samples was 78.9% in 2018, which had the highest number of unchanged samples (see Fig. 4). In addition, the proportion of unchanged samples exceeded 70% in the remaining years. The number of *C.m.* samples obtained by migration from 2016 to 2018 was only 52, 43, and 55, respectively, which was inadequate compared to the sample size for other types. As a result, a visual interpretation method was used to identify the number of *C.m.* samples from 2016 to 2018. Finally, the sample number of wetland plant communities from 2016 to 2022 is shown in Table II.

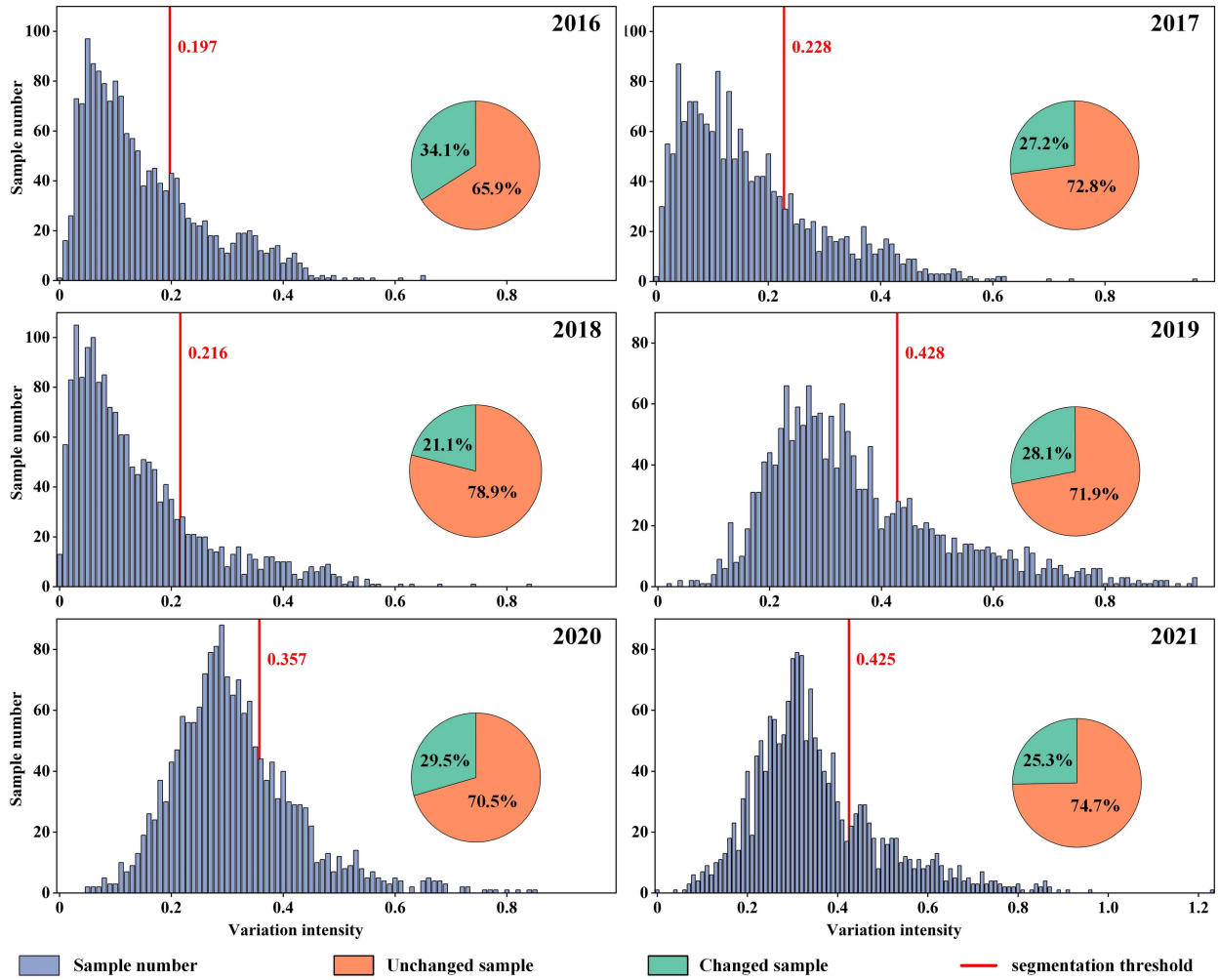

Fig. 4. Histogram of CI based on sample data from 2016 to 2021, including the proportion of migrated samples and segmentation threshold.

B. Classification Results and Accuracy Evaluation

The classification results are shown in Fig. 5. *P.a.* was mainly distributed in Zhalong Nature Reserve, *C.m.* was mainly distributed in Nen River, and *T.o.*, *S.t.*, and *S.g.* were scattered throughout the study area [see Fig. 5(a1)–(a7)]. Results of accuracy evaluation showed that the OA and Kappa coefficient gradually decreased as the sample data migrated from 2022 to 2016 (see Table III). The highest OA and kappa coefficient (OA = 93.9%, Kappa = 0.92) were obtained in 2022. The lowest OA and kappa coefficient (OA = 81.8%, Kappa = 0.77) were observed in 2016. The average OA and kappa coefficient for classification from 2016 to 2022 were 89.5% and 0.87, respectively.

C. RF Model Interpretability Based on SHAP

The bar plot provides a global perspective on model interpretation, using the absolute average of the SHAP values to determine feature importance. The results indicate that MOS_IRECI is the most important feature in determining model prediction results, followed by other features such as MOS_NDVI and DRS_NDVI [see Fig. 6(a)]. In addition, the bar plot reveals local fluctuations in the role of features in predicting different classes. In predicting *P.a.*, *T.o.*, *S.t.*, *S.g.*, and *C.m.*, the most influential features are DRS_NDVI, MOS_IRECI, SA_IRECI, BV_NDWI, and MOS_NDVI [see Fig. 6(a)]. Fig. 6(b) illustrates the importance of these features in predicting *P.a.*, displaying the impact of feature values on model output for individual samples. Notably, DRS_NDVI is particularly important in predicting *P.a.*, with higher DRS_NDVI values leading to SHAP values lower than 0, indicating a lower probability of being classified as *P.a.* [see Fig. 6(b)]. SA_IRECI and IRS_NDVI have positive effects on the prediction outcomes, whereas ELE and MOS_NDWI have negative effects [see Fig. 6(b)]. The heatmap plot shows the overall substructure of a validation sample collection sorted by the sum of SHAP values for all features when predicting *P.a.* It also shows the output of the model ($f(x)$) and the global importance of the features (bar graph on the right side of the y-axis). The most influential feature impacting the prediction result for this sample collection is DRS_IRECI, which has a positive impact on the model output [see Fig. 6(c)]. Furthermore, the results show a significant negative effect of the ELE feature on the model output for the third sample [see Fig. 6(c)]. The waterfall plot illustrates the contribution of different features

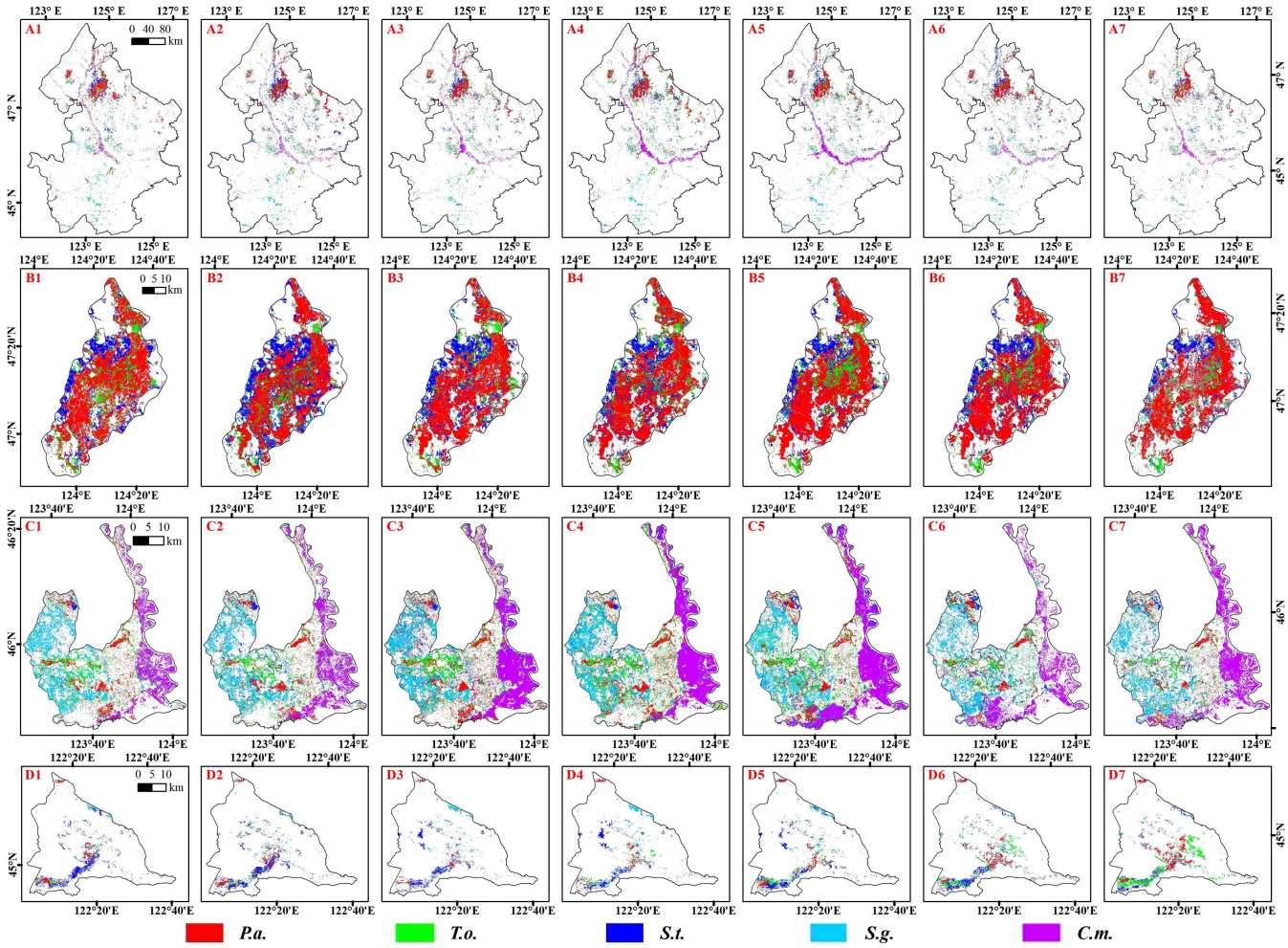

Fig. 5. Annual classification results of wetland plant communities. (a) Western Songnen Plain. (b) Zhalong Nature Reserve. (c) Momoge Nature Reserve. (d) Xianghai Nature Reserve. The serial numbers of 1–7 represent 2016–2022 years.

TABLE III
ACCURACY EVALUATION

Year	Accuracy	*P.a.*	*T.o.*	*S.t.*	*S.g.*	*C.m.*	OA	Kappa
2016	UA	81.8%	83.3%	80.2%	80.9%	84.1%	81.8%	0.77
	PA	83.7%	81.6%	83.3%	77.6%	82.2%		
2017	UA	80.7%	84.3%	83.1%	83.7%	85.1%	83.3%	0.79
	PA	85.2%	81.1%	83.1%	81.8%	85.1%		
2018	UA	89.5%	86.2%	87.2%	92.3%	93.5%	89.4%	0.87
	PA	91.9%	84.8%	89.5%	87.0%	97.7%		
2019	UA	91.3%	89.6%	90.0%	92.9%	97.8%	91.8%	0.90
	PA	91.3%	90.8%	92.3%	91.2%	93.6%		
2020	UA	92.1%	91.3%	92.2%	96.7%	96.1%	93.5%	0.92
	PA	92.1%	94.8%	94.7%	92.2%	92.5%		
2021	UA	92.2%	92.3%	94.4%	91.8%	93.8%	92.9%	0.91
	PA	92.2%	92.3%	92.4%	94.4%	93.8%		
2022	UA	94.1%	95.0%	90.1%	90.9%	97.9%	93.9%	0.92
	PA	93.0%	93.8%	91.4%	93.8%	96.8%		

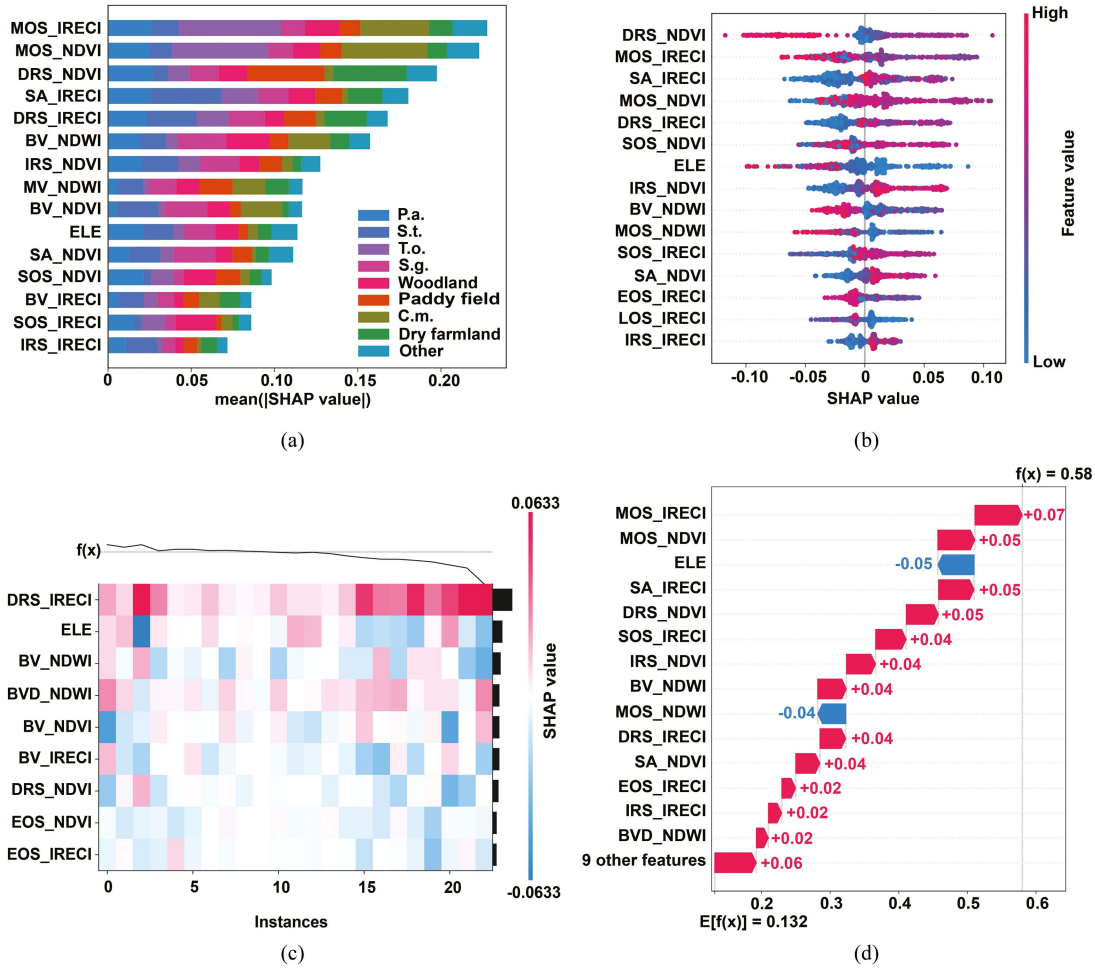

Fig. 6. Interpretability of the RF model. (a) Bar plot. (b) Beeswarm plot. (c) Heatmap plot. (d) Waterfall plot.

within the model when classifying a given sample as *P.a.* The results reveal that ELE and MOS_NDWI have a negative gain for predicting this sample, while the feature with the largest positive gain is MOS_IRECI [see Fig. 6(d)].

D. Spatiotemporal Changes of Wetland Plant Communities

Fig. 7(a) shows the changes in area and DD of the dominant wetland plant communities in the western Songnen Plain from 2016 to 2022. In general, *P.a.* had the smallest annual DD in the study area, while *C.m.* had the largest annual DD. The distribution of *P.a.* remained relatively stable from 2016 to 2022, while that of *C.m.* was highly variable. The areas of *P.a.*, *T.o.*, and *C.m.* showed an increasing and then decreasing trend in the western Songnen Plain. Fig. 8(a1)–(a3) shows that the CIs of wetland plant communities varied by type and region. Except for the low CI of *P.a.* in and near Zhalong Nature Reserve, the CI of *P.a.* was relatively high in other areas. The CI of *T.o.* was low in Chagan Lake, while the CI of *T.o.* was relatively high in other areas. Similarly, the CI of *C.m.* was weak in Momoge Nature Reserve, whereas the CI of *C.m.* was relatively strong in other areas.

S.g. and *C.m.* are sparsely distributed in Zhalong Nature Reserve. Therefore, only the spatiotemporal evolution characteristics of *P.a.*, *T.o.*, and *S.t.* were analyzed in Zhalong Nature Reserve. All three species showed different DDs, with the annual DD of *P.a.* being the smallest, while that of *T.o.* and *S.t.* were larger, indicating that *P.a.* was more stable than *T.o.* and *S.t.* from 2016 to 2022 [see Fig. 7(b)]. Moreover, the area of *P.a.* showed an initial increase followed by a decrease, while the areas of *T.o.* and *S.t.* generally showed a gradual decreasing trend. The evolution of *P.a.* mainly occurred in the peripheral areas of the communities [see Fig. 8(b1)]. The increase in *P.a.* was primarily due to the evolution of *T.o.* and *S.t.* into *P.a.* in the eastern Zhalong Nature Reserve. The disappearance of *P.a.* in the central part of the reserve and the evolution of *P.a.* into *T.o.* in the southern part of the reserve resulted in a decrease in the area of *P.a.* The weakest CI of *T.o.* was observed in the eastern part of the Dongsheng reservoir and the southern part of the reserve, indicating that the distribution of *T.o.* was highly stable in these areas [see Fig. 8(b2)]. *S.t.* in the eastern part of the reserve exhibited a gradual disappearance around 2018, whereas the range of *S.t.* in the western part of the reserve continued to shrink [see Fig. 5(b1)–(b7)].

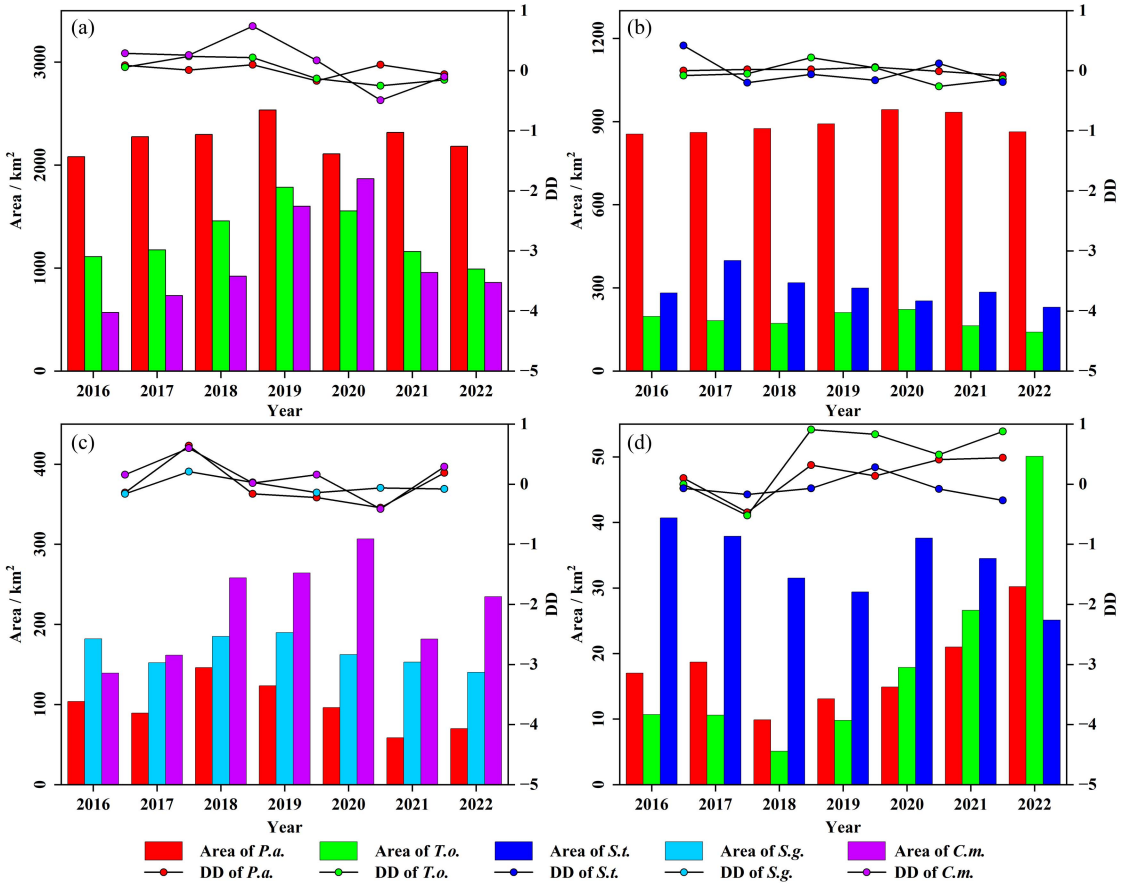

Fig. 7. Annual changes in area and DD of typical wetland plant communities in the western Songnen Plain and three Ramsar wetlands from 2016 to 2022. (a) Western Songnen Plain. (b) Zhalong Nature Reserve. (c) Momoge Nature Reserve. (d) Xianghai Nature Reserve.

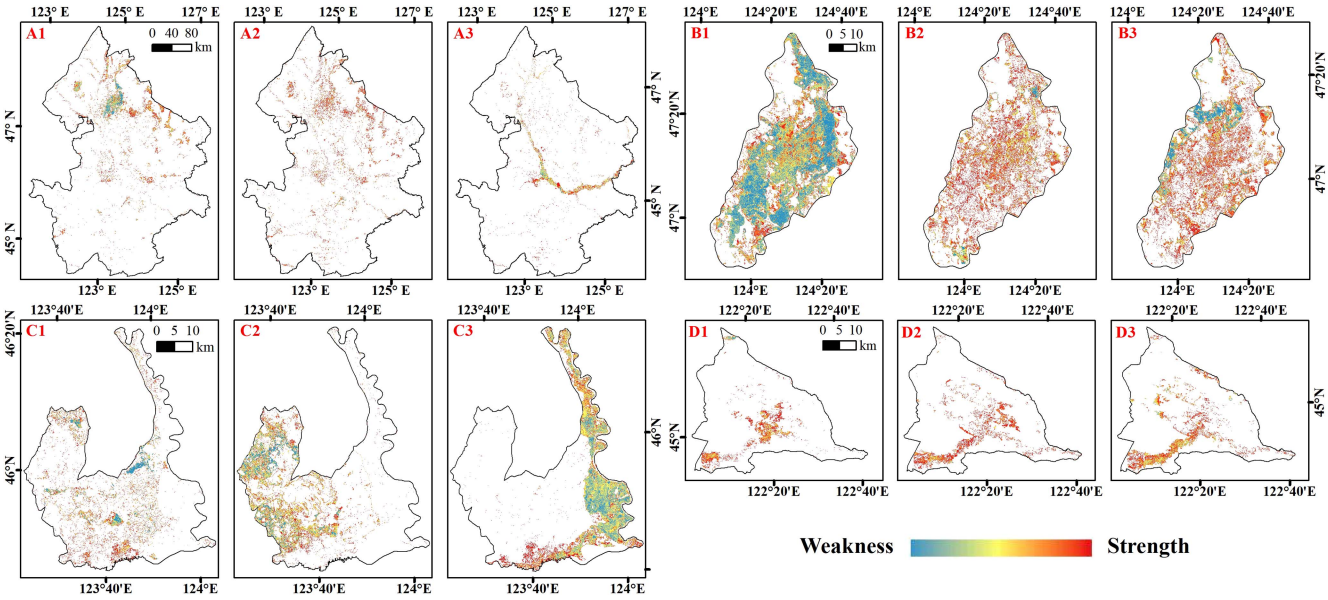

Fig. 8. CI of wetland plant communities from 2016 to 2022. (a1)–(a3) Results of *P.a.*, *T.o.*, and *C.m.* of western Songnen Plain. (b1)–(b3) Results of *P.a.*, *T.o.*, and *S.t.* of Zhalong Nature Reserve. (c1)–(c3) Results of *P.a.*, *S.g.*, and *C.m.* of Momoge Nature Reserve. (d1)–(d3) Results of *P.a.*, *T.o.*, and *S.t.* of Xianghai Nature Reserve.

The main wetland plant communities are *P.a.*, *S.g.*, and *C.m.* in Momoge Nature Reserve. Overall, *S.g.* had the smallest annual DD, whereas *P.a.* and *C.m.* had larger DD [see Fig. 7(c)]. The area changes of *P.a.* generally showed a gradually decreasing trend, whereas the opposite was true for *C.m*. In addition, the area of *S.g.* first increased and then decreased. The decrease in *P.a.* mainly occurred in areas such as Baihe Lake and Weihai Village [see Fig. 8(c1)]. The CI of *S.g.* was weak in the northwestern part of the reserve, whereas the change of *S.g.* was more severe in the southwestern part of the reserve [see Fig. 8(c2)]. Since 2019, the distribution of *S.g.* showed an overall shrinking trend, resulting in a continuous decrease in area from year to year [see Fig. 5(c1)–(c7)]. The CI of *C.m.* was weak in the Nen River floodplain and Moon Lake, whereas the CI of *C.m.* along the Taoer River was relatively strong [see Fig. 8(c3)].

The dominant wetland plant communities are *P.a.*, *T.o.*, and *S.t.* in Xianghai Nature Reserve. Overall, *S.t.* had the smallest annual DD, whereas *P.a.* and *T.o.* had larger DD [see Fig. 7(d)]. The area changes of *P.a.* generally showed a gradually increasing trend, whereas the opposite was true for *S.t*. In addition, the area of *T.o.* first decreased and then increased. The weakest CI of *P.a.* was observed in the Hucanggou reservoir, whereas the CI of *P.a.* in other areas was larger, especially at the intersection of Huolin River and Xinglong reservoir [see Fig. 8(d1)]. Generally, the overall CI of *T.o.* was high, and the increase in *T.o.* primarily occurred at the intersection and in the Huolin River in the southwest of the reserve [see Fig. 8(d2)]. The area of *S.t.* in the Huolin River exhibited a continuous decrease from 2016 to 2022 [see Fig. 8(d3)]. Moreover, while the area of *S.t.* in the western Xianghai Nature Reservoir continued to increase from 2016 to 2019, it gradually decreased since 2020 [see Fig. 5(d1)–(d7)].

IV. Discussion

A. Challenges of Community-Scale Sample Migration

The basic principles of sample migration are similar, but the challenge of community-scale sample migration lies in its higher demands on data and methodology. Obtaining accurate and sufficient reference samples is a critical requirement for community-scale sample migration. Traditional spectral image interpretation, based on features such as color, texture, and shape, can effectively obtain samples of land cover types with significant differences. Some studies attempt to identify seasonal differences from multitemporal remote sensing images to improve the discrimination between land cover types with similar spectral features for more accurate visual interpretation [16]. In addition to using multitemporal remote sensing images, a pixel-based annual NDVI time-series curve was incorporated as a reference, to facilitate identification of different wetland plant communities. Nevertheless, due to factors such as the complexity of wetland environments and differences in vegetation health, visual interpretation of wetland plant community sample data remains challenging and time-consuming.

In addition, obtaining images from the source and target domains with consistent radiometric conditions is a key factor affecting the effectiveness of community-scale sample migration. Despite efforts to eliminate atmospheric and radiometric differences between different years, some issues persist. For instance, the intensity peaks and segmentation thresholds of the sample migration results from 2016–2018 are smaller than those from 2019–2021 (see Fig. 4), which contradicts the general assumption that the likelihood of change increases with a longer time interval. The main reason for this discrepancy is the use of Sentinel-2 L1C images for 2016–2018, which were not atmospherically corrected. Atmospheric absorption and scattering effects degrade image quality, attenuating changes in spectral information on L1C images [57]. Although the median reduction is considered an effective method for reducing radiometric differences, it may not perform well when the number of images is small or there are numerous cloud pixels. While the CVA method used in this study has the advantage of simplicity and convenience, some studies suggest that this distance-based method may not provide effective samples for wetland mapping [33]. Future research can continue to explore the applicability of other migration methods for community-scale sample migration, such as the isolated forest algorithm [58].

It is important to perform accuracy verification on migrated samples. While some studies have used visual interpretation [59], at the community scale, this can be very challenging. The most direct and effective approach is to cross-validate historical year classification results with migration and survey samples [60]. However, due to the lack of wetland survey data, currently only survey samples can be used for verification at Momoge Nature Reserve in 2020 [20]. Here, we used survey samples to verify the accuracy of migration classification results (SSA) and used migration samples to verify the accuracy of survey classification results (MSA). The results showed that the SSA of *P.a.*, *S.g.*, and *C.m.* were 80.0%, 96.6%, and 100%, respectively, and the MSA of *P.a.* and *C.m.* were 89.5% and 92.1% respectively. This result illustrates the effectiveness of the sample migration method used in this study. It should be noted that the SSA of *T.o.* and *S.t.* were not calculated, and the MSA of *T.o.*, *S.t.*, and *S.g.* were also not calculated. They have no statistical significance, due to the limited sample number or community area. Finally, as a method of improvement, we believe that a wetland survey every 5 years is necessary. This would allow more survey samples to achieve better sample migration between two survey years and enhance system reliability.

B. Interpretability of Features and Model Based on SHAP

The importance evaluation results of the RF model in 2022 show that MOS_NDVI, MV_NDWI, SA_IRECI, MOS_IRECI, SA_NDVI, and BV_NDWI are important features, which conform to the results explained by the SHAP model [see Fig. 6(a)]. Despite the relatively high importance of ELE in the SHAP model interpretation results [see Fig. 6(b)–(d)], it does not play a prominent role in each prediction class [see Fig. 6(a)]. *P.a.* shows a slower yellowing trend than other wetland plant communities, which is manifested in a smaller DRS_NDVI in the NDVI time-series curve. Prior research has indicated that the IRECI time-series curves for *P.a.* fluctuate more significantly than those of other wetland plant communities [20], making

samples with larger SA_IRECI more likely to be predicted as *P.a.* [see Fig. 6(b)].

It is crucial to interpret a trained model in a human-understandable way, which helps to assess its reliability, understand its internal logic, and evaluate feature importance [61]. The SHAP model has the advantage of providing a more comprehensive interpretation of the internal logic of the model. In this study, the SHAP model revealed differences in the role of each feature in distinguishing different classes. It also meticulously analyzed the impact of the magnitude of each feature value on predicting a particular class. In addition, the SHAP model can analyze the internal substructure of a sample collection and the predictive logic of an individual sample for a specific class. It is worth noting that when there are strong interactions between features, the SHAP model may provide misleading estimates of feature importance [62]. This study also suggests that there may be differences in the interpretation of the SHAP model at the global and local levels (see Fig. 6). This is because the global interpretation reflects the average patterns of the entire validation sample collection, whereas subsets of samples and individual samples may exhibit unique patterns.

C. Factors Affecting Spatiotemporal Changes in Wetland Plant Communities

The spatiotemporal change characteristics of the distribution of different wetland plant communities can not only reflect wetland health, ecology, hydrology, and land use changes but also help managers detect wetland degradation and the effectiveness of wetland protection measures promptly [20]. This study shows that the main wetland plant communities increased from 2016 to 2019, and decreased significantly from 2020 to 2022 in the western Songnen Plain [see Fig. 7(a)]. This cannot be considered evidence of poor wetland protection efforts. On the contrary, it fully reflects the severe challenges of climate factors (e.g., extreme precipitation events) to wetland protection efforts. Precipitation changes surface hydrologic conditions and water quality, and surface water confluence leads to high incidence of wetland flooding, thereby affecting community evolution [31], [63]. In 2021 and 2022, there was significantly more precipitation in the Nen River basin and western Jilin [64], and the flood season lasted from early June to early September. As a result, the water levels of the Nen River and the Taoer River remained high, and the water level of the previously dry Huolin River rose significantly. Extreme climatic events, such as heavy rainfall, triggered flooding of wetland vegetation, resulting in drastic changes in wetland areas [65]. In addition, the increasing requirements for living space and quality brought about by population growth and socioeconomic development have also profoundly affected the evolution of wetlands [66]. Nonpoint source pollution from animal husbandry and agricultural activities was the most important factor affecting the water quality of Xianghai Lake [67]. Affected by intensive human activities in the vicinity, such as agricultural irrigation and domestic sewage discharge, the water volume and quality of the lakes have decreased in the southern Zhalong Nature Reserve, resulting in the shrinkage and fragmentation of wetlands [68], [69].

The government has carried out ecological engineering construction projects (e.g., returning farmland to wetland and river-lake connection), and wetlands have been restored in Xianghai lake, Taoer river, and Huolin river to a certain extent [70], [71]. However, simple and crude hydrological control measures are not always beneficial to wetland protection. For example, excessively high water levels will lead to the continuous reduction of the living space of *S.t.* community [20]. Considering the impact difference of natural and human factors on wetlands in long-term and short-term studies [63], different recommendations for wetland protection in the western Songnen Plain were put forward. From a long-term perspective, managers should continue to strengthen the construction of wetland protection areas, promote the implementation of wetland protection projects, and discuss the construction of wetland national parks. The optimization of the "One Belt, Two Screens, Four Zones, Six Groups, and Multiple Nodes" ecological security pattern has the advantages of regional coordination and multiple measures, which provides new ideas for the sustainable protection of wetlands in the western Songnen Plain [72]. Focusing on the present, managers should improve the real-time monitoring system of wetland water conditions, formulate temporary response mechanisms to deal with emergency hydrological events, and scientifically design water storage and drainage flow plans as soon as possible [67]. It helps ensure the stability of wetland ecosystem structure.

V. Conclusion

By utilizing the sample data obtained through the sample migration method based on CVA after K-T transformation, combined with Sentinel-1/2 time-series and DEM data, a 10-m resolution wetland plant community map of the western Songnen Plain from 2016 to 2022 was generated based on the RF model. By incorporating various phenological and time-series features into the fine classification of wetlands, the classification accuracy was further improved, achieving an average overall accuracy of 89.5% and an average kappa coefficient of 0.87. The wetland plant communities in the western Songnen Plain and three national nature reserves show distinct spatiotemporal change characteristics. *P.a.* represents the most widespread and least variable community type in the western Songnen Plain. The community distribution in the Zhalong Nature Reserve is the most stable, whereas the community distribution in the Xianghai Nature Reserve undergoes the most dramatic changes from 2016 to 2022. The dual impacts of climate change and human activities contribute to the diverse spatiotemporal change characteristics of wetland plant communities. This study provides valuable data support for the fine and sustainable management of wetland resources in the western Songnen Plain and related wetland ecology research.

Acknowledgment

The authors are very grateful to GEE (https://earthengine.google.com/) and PIE-Engine (https://engine.piesat.cn) for providing free services. The authors would like to thank Mr. Y. An and Mr. Z. Wang for their help in the field survey. Finally, the authors sincerely thank the editor and reviewers for their time

and effort in providing detailed comments that helped improve the quality of this article.

REFERENCES

[1] M. Kelly and K. Tuxen, "Remote sensing support for tidal wetland vegetation research and management," in *Remote Sensing and Geospatial Technologies For Coastal Ecosystem Assessment and Management*, X. Yang, Ed., in Lecture Notes in Geoinformation and Cartography. Berlin, Germany: Springer, 2009, pp. 341–363.

[2] M. S. Vanderlinder, C. M. U. Neale, D. E. Rosenberg, and K. M. Kettenring, "Use of remote sensing to assess changes in wetland plant communities over an 18-year period: A case study from the Bear River migratory Bird Refuge, Great Salt Lake, Utah," *Western North Amer. Naturalist*, vol. 74, no. 1, pp. 33–46, Jun. 2014.

[3] I. Caçador, J. M. Neto, B. Duarte, D. V. Barroso, M. Pinto, and J. C. Marques, "Development of an Angiosperm Quality Assessment Index (AQuA-Index) for ecological quality evaluation of Portuguese water bodies—A multi-metric approach," *Ecological Indicators*, vol. 25, pp. 141–148, Feb. 2013.

[4] J. Martínez-López, M. F. Carreño, J. A. Palazón-Ferrando, J. Martínez-Fernández, and M. A. Esteve, "Remote sensing of plant communities as a tool for assessing the condition of semiarid Mediterranean saline wetlands in agricultural catchments," *Int. J. Appl. Earth Obs. Geoinf.*, vol. 26, pp. 193–204, Feb. 2014.

[5] M. K. Butera, "Remote sensing of wetlands," *IEEE Trans. Geosci. Remote Sens.*, vol. GE-21, no. 3, pp. 383–392, Jul. 1983.

[6] M. S. Gilmore et al., "Integrating multi-temporal spectral and structural information to map wetland vegetation in a lower Connecticut River tidal marsh," *Remote Sens. Environ.*, vol. 112, no. 11, pp. 4048–4060, Nov. 2008.

[7] R. D. Ward, N. G. Burnside, C. B. Joyce, and K. Sepp, "The use of medium point density LiDAR elevation data to determine plant community types in Baltic coastal wetlands," *Ecological Indicators*, vol. 33, pp. 96–104, Oct. 2013.

[8] A. R. Da Silva et al., "Multi-source remote sensing recognition of plant communities at the reach scale of the Vistula River, Poland," *Ecological Indicators*, vol. 142, pp. 109160, Sep. 2022.

[9] S. Mahdavi, B. Salehi, J. Granger, M. Amani, B. Brisco, and W. Huang, "Remote sensing for wetland classification: A comprehensive review," *GISci. Remote Sens.*, vol. 55, no. 5, pp. 623–658, Sep. 2018.

[10] B. Fu et al., "Combination of super-resolution reconstruction and SGA-Net for marsh vegetation mapping using multi-resolution multispectral and hyperspectral images," *Int. J. Digit. Earth*, vol. 16, no. 1, pp. 2724–2761, Oct. 2023.

[11] S. Bhatnagar, L. Gill, and B. Ghosh, "Drone image segmentation using machine and deep learning for mapping raised bog vegetation communities," *Remote Sens.*, vol. 12, no. 16, Aug. 2020, Art. no. 2602.

[12] M. Laba et al., "Use of textural measurements to map invasive wetland plants in the Hudson River National Estuarine Research Reserve with IKONOS satellite imagery," *Remote Sens. Environ.*, vol. 114, no. 4, pp. 876–886, Apr. 2010.

[13] N. Li, G. Xie, D. Zhou, C. Zhang, and C. Jiao, "Remote sensing classification of marsh wetland with different resolution images," *J. Resour. Ecol.*, vol. 7, no. 2, pp. 107–114, Mar. 2016.

[14] C. L. Zweig, M. A. Burgess, H. F. Percival, and W. M. Kitchens, "Use of unmanned aircraft systems to delineate fine-scale wetland vegetation communities," *Wetlands*, vol. 35, no. 2, pp. 303–309, Apr. 2015.

[15] M. Mahdianpari, B. Salehi, F. Mohammadimanesh, S. Homayouni, and E. Gill, "The first wetland inventory map of Newfoundland at a spatial resolution of 10 m using Sentinel-1 and Sentinel-2 data on the Google Earth Engine cloud computing platform," *Remote Sens.*, vol. 11, no. 1, Dec. 2018, Art. no. 43.

[16] Z. Qiu, D. Mao, K. Feng, M. Wang, H. Xiang, and Z. Wang, "High-resolution mapping changes in the invasion of *Spartina Alterniflora* in the Yellow River Delta," *IEEE J. Sel. Topics Appl. Earth Observ. Remote Sens.*, vol. 15, pp. 6445–6455, Jul. 2022.

[17] M. D. Correll et al., "Fine-scale mapping of coastal plant communities in the northeastern USA," *Wetlands*, vol. 39, no. 1, pp. 17–28, 2019.

[18] P. A. Townsend and S. J. Walsh, "Remote sensing of forested wetlands: Application of multitemporal and multispectral satellite imagery to determine plant community composition and structure in southeastern USA," *Plant Ecol.*, vol. 157, pp. 129–149, Dec. 2001.

[19] T. S. F. Silva, M. P. F. Costa, J. M. Melack, and E. M. L. M. Novo, "Remote sensing of aquatic vegetation: Theory and applications," *Environ. Monit. Assessment*, vol. 140, no. 1–3, pp. 131–145, May 2008.

[20] K. Feng, D. Mao, Z. Qiu, Y. Zhao, and Z. Wang, "Can time-series Sentinel images be used to properly identify wetland plant communities?," *GISci. Remote Sens.*, vol. 59, no. 1, pp. 2202–2216, Dec. 2022.

[21] C. Sun, J. Li, Y. Liu, Y. Liu, and R. Liu, "Plant species classification in salt marshes using phenological parameters derived from Sentinel-2 pixel-differential time-series," *Remote Sens. Environ.*, vol. 256, Apr. 2021, Art. no. 112320.

[22] Y. Hu et al., "Mapping coastal salt marshes in China using time series of Sentinel-1 SAR," *ISPRS J. Photogramm. Remote Sens.*, vol. 173, pp. 122–134, Mar. 2021.

[23] M. Amani, B. Salehi, S. Mahdavi, and B. Brisco, "Spectral analysis of wetlands using multi-source optical satellite imagery," *ISPRS J. Photogramm. Remote Sens.*, vol. 144, pp. 119–136, Oct. 2018.

[24] J. A. Dechka, S. E. Franklin, M. D. Watmough, R. P. Bennett, and D. W. Ingstrup, "Classification of wetland habitat and vegetation communities using multi-temporal Ikonos imagery in southern Saskatchewan," *Can. J. Remote Sens.*, vol. 28, no. 5, pp. 679–685, Oct. 2002.

[25] Z. Szantoi, F. J. Escobedo, A. Abd-Elrahman, L. Pearlstine, B. Dewitt, and S. Smith, "Classifying spatially heterogeneous wetland communities using machine learning algorithms and spectral and textural features," *Environ. Monit. Assessment*, vol. 187, no. 5, May 2015, Art. no. 262.

[26] T. Hoeser and C. Kuenzer, "Object detection and image segmentation with Deep learning on Earth observation data: A review-part I: Evolution and recent trends," *Remote Sens.*, vol. 12, no. 10, May 2020, Art. no. 1667.

[27] L. Deng et al., "Comparison of 2D and 3D vegetation species mapping in three natural scenarios using UAV-LiDAR point clouds and improved deep learning methods," *Int. J. Appl. Earth Obs. Geoinf.*, vol. 125, Dec. 2023, Art. no. 103588.

[28] V. S. Martins, A. L. Kaleita, B. K. Gelder, G. W. Nagel, and D. A. Maciel, "Deep neural network for complex open-water wetland mapping using high-resolution WorldView-3 and airborne LiDAR data," *Int. J. Appl. Earth Obs. Geoinf.*, vol. 93, Dec. 2020, Art. no. 102215.

[29] B. Gregorutti, B. Michel, and P. Saint-Pierre, "Correlation and variable importance in random forests," *Comput. Statist.*, vol. 27, no. 3, pp. 659–678, May 2017.

[30] U. Nguyen, E. P. Glenn, T. D. Dang, and L. T. H. Pham, "Mapping vegetation types in semi-arid riparian regions using random forest and object-based image approach: A case study of the Colorado River Ecosystem, Grand Canyon, Arizona," *Ecol. Inf.*, vol. 50, pp. 43–50, Mar. 2019.

[31] M. Jia et al., "Tracking long-term floodplain wetland changes: A case study in the China side of the Amur River Basin," *Int. J. Appl. Earth Obs. Geoinf.*, vol. 92, Oct. 2020, Art. no. 102185.

[32] M. Jia et al., "Mapping China's mangroves based on an object-oriented classification of Landsat imagery," *Wetlands*, vol. 34, no. 2, pp. 277–283, Apr. 2014.

[33] M. Wang et al., "Wetland mapping in East Asia by two-stage object-based random forest and hierarchical decision tree algorithms on Sentinel-1/2 images," *Remote Sens. Environ.*, vol. 297, Nov. 2023, Art. no. 113793.

[34] X. Zhang et al., "GWL_FCS30: A global 30 m wetland map with a fine classification system using multi-sourced and time-series remote sensing imagery in 2020," *Earth Syst. Sci. Data*, vol. 15, no. 1, pp. 265–293, Jan. 2023.

[35] Y. Zhang et al., "Effects of multi-growth periods UAV images on classifying karst wetland vegetation communities using object-based optimization stacking algorithm," *Remote Sens.*, vol. 15, no. 16, Aug. 2023, Art. no. 4003.

[36] E. Fekri, H. Latifi, M. Amani, and A. Zobeidinezhad, "A training sample migration method for wetland mapping and monitoring using Sentinel data in Google Earth Engine," *Remote Sens.*, vol. 13, no. 20, Oct. 2021, Art. no. 4169.

[37] W. A. Malila, "Change vector analysis: An approach for detecting forest changes with Landsat," in *Proc. LARS Symposia*, 1980, Paper 385.

[38] H. Pan et al., "Updating of land cover maps and change analysis using GlobeLand30 product: A case study in Shanghai Metropolitan area, China," *Remote Sens.*, vol. 12, no. 19, Sep. 2020, Art. no. 3147.

[39] A. Singh, "Review article digital change detection techniques using remotely-sensed data," *Int. J. Remote Sens.*, vol. 10, no. 6, pp. 989–1003, 1989.

[40] D. Lu, P. Mausel, E. Brondizio, and E. Moran, "Change detection techniques," *Int. J. Remote Sens.*, vol. 25, no. 12, pp. 2365–2401, 2004.

[41] R. J. DeRose, J. N. Long, and R. D. Ramsey, "Combining dendrochronological data and the disturbance index to assess Engelmann spruce mortality caused by a spruce beetle outbreak in southern Utah, USA," *Remote Sens. Environ.*, vol. 115, no. 9, pp. 2342–2349, Sep. 2011.

[42] J. Rogan, J. Franklin, and D. A. Roberts, "A comparison of methods for monitoring multitemporal vegetation change using Thematic Mapper imagery," *Remote Sens. Environ.*, vol. 80, no. 1, pp. 143–156, Apr. 2002.

[43] B. Wen, X. Liu, X. Li, F. Yang, and X. Li, "Restoration and rational use of degraded saline reed wetlands: A case study in western Songnen Plain, China," *Chin. Geographical Sci.*, vol. 22, no. 2, pp. 167–177, Apr. 2012.

[44] Y. Zhong, Z. Xue, M. Jiang, B. Liu, and G. Wang, "The application of species distribution modeling in wetland restoration: A case study in the Songnen Plain, Northeast China," *Ecological Indicators*, vol. 121, Feb. 2021, Art. no. 107137.

[45] Y. Tian et al., "Remote observation in habitat suitability changes for waterbirds in the West Songnen Plain, China," *Sustainability*, vol. 11, no. 6, pp. 1552, Mar. 2019.

[46] C. He, Y. Song, H. Lang, H. Li, and X. Sun, "Migratory dynamics of Siberian crane and environmental conditions at its stop-over site," *Biodiversity Conservation*, vol. 10, no. 3, pp. 286–290, Feb. 2002.

[47] D. Liu et al., "Potential natural exposure of endangered red-crowned crane (Grus japonensis) to mycotoxins aflatoxin B1, deoxynivalenol, zearalenone, T-2 toxin, and ochratoxin A," *J. Zhejiang Univ.-Sci. B*, vol. 17, no. 2, pp. 158–168, Feb. 2016.

[48] G. Wang et al., "A multiscale approach to identifying spatiotemporal pattern of habitat selection for red-crowned cranes," *Sci. Total Environ.*, vol. 739, pp. 139980, Oct. 2020.

[49] Z. Dong et al., "Assessment of habitat suitability for waterbirds in the West Songnen Plain, China, using remote sensing and GIS," *Ecol. Eng.*, vol. 55, pp. 94–100, Jun. 2013.

[50] M. Amani et al., "A generalized supervised classification scheme to produce provincial wetland inventory maps: An application of Google Earth Engine for big geo data processing," *Big Earth Data*, vol. 3, no. 4, pp. 378–394, Nov. 2019.

[51] B. Wu, Y. Tian, and Q. Li, "GVG, a crop type proportion sampling instrument," *J. Remote Sens.*, no. 6, pp. 570–580, Nov. 2004.

[52] N. Otsu, "A threshold selection method from gray-level histograms," *IEEE Trans. Syst. Man Cybern.*, vol. 9, no. 1, pp. 62–66, Jan. 1979.

[53] Z. Zhen, L. J. Quackenbush, S. V. Stehman, and L. Zhang, "Impact of training and validation sample selection on classification accuracy and accuracy assessment when using reference polygons in object-based classification," *Int. J. Remote Sens.*, vol. 34, no. 19, pp. 6914–6930, Oct. 2013.

[54] S. M. Lundberg and S.-I. Lee, "A unified approach to interpreting model predictions," *Adv. Neural Inf. Process. Syst.*, vol. 30, pp. 4768–4777, 2017.

[55] S. M. Lundberg et al., "From local explanations to global understanding with explainable AI for trees," *Nature Mach. Intell.*, vol. 2, no. 1, pp. 56–67, Jan. 2020.

[56] H. Zhu, X. Li, S. He, and M. Zhang, "Spatio-temporal change of land use in Bohai Rim," *Acta Geologica Sinica*, vol. 56, no. 3, pp. 253–260, May 2001.

[57] X. Qi and Q. Tian, "The advances in the study of atmospheric correction for optical remote sensing," *Remote Sens. Nat. Resour.*, no. 4, pp. 1–6, Dec. 2005.

[58] B. Fu et al., "Performance evaluation of backscattering coefficients and polarimetric decomposition parameters for marsh vegetation mapping using multi-sensor and multi-frequency SAR images," *Ecological Indicators*, vol. 157, pp. 111246, Dec. 2023.

[59] X. Yan and Z. Niu, "Reliability evaluation and migration of wetland samples," *IEEE J. Sel. Topics Appl. Earth Obs. Remote Sens.*, vol. 14, pp. 8089–8099, 2021.

[60] Q. Zhu, Y. Wang, J. Liu, X. Li, H. Pan, and M. Jia, "Tracking historical wetland changes in the China side of the Amur River Basin based on landsat imagery and training samples migration," *Remote Sens.*, vol. 13, no. 11, May 2021, Art. no. 2161.

[61] B. Fu et al., "Quantifying scattering characteristics of mangrove species from Optuna-based optimal machine learning classification using multi-scale feature selection and SAR image time series," *Int. J. Appl. Earth Obs. Geoinf.*, vol. 122, Aug. 2023, Art. no. 103446.

[62] J. Mi, A. Li, and L. Zhou, "Review study of interpretation methods for future interpretable machine learning," *IEEE Access*, vol. 8, pp. 191969–191985, 2020.

[63] C. Song, H. S. He, K. Liu, H. Du, and J. Krohn, "Impact of historical pattern of human activities and natural environment on wetland in Heilongjiang River Basin," *Front. Environ. Sci. Eng.*, vol. 17, no. 12, Dec. 2023, Art. no. 151.

[64] X. Zhang, "Analysis on the heavy rain weather process in most areas of China from July 26 to 30, 2022," *J. Geosci. Environ. Prot.*, vol. 11, no. 01, pp. 183–188, Jan. 2023.

[65] Y. Xiong, S. Mo, H. Wu, X. Qu, Y. Liu, and L. Zhou, "Influence of human activities and climate change on wetland landscape pattern—A review," *Sci. Total Environ.*, vol. 879, Jun. 2023, Art. no. 163112.

[66] D. Mao et al., "Conversions between natural wetlands and farmland in China: A multiscale geospatial analysis," *Sci. Total Environ.*, vol. 634, pp. 550–560, Sep. 2018.

[67] J. Gao et al., "Water quality management of micro swamp wetland based on the 'source-transfer-sink' theory: A case study of Momoge Swamp Wetland in Songnen Plain, China," *J. Clean. Prod.*, vol. 446, Mar. 2024, Art. no. 141450.

[68] C. Lu, Z. Wang, M. Liu, L. Ouyang, M. Jia, and D. Mao, "Analysis of conservation effectiveness of wetland protected areas based on remote sensing in West Songnen Plain," *China Environ. Sci.*, vol. 35, no. 2, pp. 599–609, Mar. 2015.

[69] Y. Zhong, Z. Xue, M. Jiang, B. Liu, and G. Wang, "The application of species distribution modeling in wetland restoration: A case study in the Songnen Plain, Northeast China," *Ecological Indicators*, vol. 121, Feb. 2021, Art. no. 107137.

[70] B. Peng, J. Yang, Y. Li, and S. Zhang, "Land use/Land cover changes in Baicheng District, China during the period 1954–2020 and their driving forces," *Land*, vol. 12, no. 10, Sep. 2023, Art. no. 1845.

[71] D. Li et al., "The influence of ecological engineering on waterbird diversity in different habitats within the Xianghai Nature Reserve," *Diversity*, vol. 14, no. 12, Nov. 2022, Art. no. 1016.

[72] J. Liu, B. Chen, M. Zhang, D. Wan, and X. Liu, "Construction and optimization of ecological security patterns in the Songnen plain," *Front. Environ. Sci.*, vol. 12, Jan. 2024, Art. no. 1302896.